PROCEEDINGS, 51st Workshop on Geothermal Reservoir Engineering
Stanford University, Stanford, California, February 9-11, 2026
SGP-TR-230

Experimental Investigation of Thermal Shock Effects on Fracture Nucleation and Propagation of Igneous Rocks

Touka ELSAYED, Francisca NOIJA, Evan KIAS, Esuru Rita OKOROAFOR

[1]Texas A&M University, [2]W D Von Gonten Engineering LLC

touka@tamu.edu

Keywords: Igneous rocks, Granite, Ultramafic rock, thermal shock, Micro-CT, UCS, Young's modulus, THM coupling, enhanced geothermal systems

ABSTRACT

The thermo-mechanical response of igneous rocks to rapid temperature fluctuations governs both the heat-extraction efficiency in Enhanced Geothermal Systems (EGS) and the permeability development in engineered geological hydrogen systems. This study experimentally investigated the effects of thermal shock on the strength, stiffness, and fracture evolution of granite and ultramafic rocks to establish cross-domain insights into subsurface energy systems.

Cylindrical granite and ultramafic specimens were characterized using micro-computed tomography (micro-CT) measurements, then subjected to controlled thermal shock treatments consisting of heating to 200 °C followed by rapid quenching in water at 0 °C or 20 °C to simulate cold-fluid injection into hot geothermal reservoirs. Micro-CT analysis reveals systematic porosity increases following thermal treatment, with heating alone producing minor increases of ~0.07–0.43 percentage points, while rapid quenching results in substantially larger porosity gains of up to ~1.0 percentage point in granite and ~0.8 percentage points in ultramafic samples. These microstructural changes are accompanied by reductions in elastic stiffness, with P- and S-wave velocities decreasing by approximately 5–15% and Young's modulus decreasing by ~15–40% depending on lithology and quenching severity. Granite exhibits larger relative porosity increases and greater stiffness degradation under thermal shock, whereas ultramafic samples retain higher absolute velocities and moduli, indicating greater resistance to thermally induced damage. Together, the porosity–velocity–modulus response provides experimentally constrained insight into thermally driven fracture evolution and its role in permeability enhancement in enhanced geothermal systems.

1. INTRODUCTION

Enhanced Geothermal Systems (EGS) rely on engineered stimulation of hot, low-permeability crystalline formations to enable sustainable heat extraction (Tester et al., 2006; Yehia et al., 2024; Duchane & Brown, 2002). In contrast to natural geothermal systems, where permeability and fluid pathways are pre-existing, EGS operations depend on mechanical and thermal processes to generate and maintain fracture networks within strong igneous rocks such as granite (McClure & Horne, 2014; Zoback et al., 2012). Among these processes, thermal shock induced by cold-fluid injection into hot rock plays a critical role in controlling fracture nucleation, stiffness degradation, and permeability evolution (Siratovich et al., 2015).

Typical EGS reservoirs reach temperatures of 150–250 °C, while injected fluids may be near ambient or even near-freezing conditions (Tester et al., 2006). This large temperature contrast generates intense thermo-elastic stresses due to rapid and spatially nonuniform mineral contraction (Fredrich & Wong, 1986). In polymineralic rocks, differences in thermal expansion coefficients between quartz, feldspar, and mica phases promote microcrack initiation along grain boundaries and pre-existing defects (Griffiths et al., 2018). These thermally induced microcracks can significantly alter elastic properties, fracture connectivity, and the mechanical integrity of the reservoir (Heap et al., 2014; Siratovich et al., 2014).

This behavior of thermally induced microcracks is relevant to ultramafic rocks where research is ongoing to create fractures that allow water-rock reaction for hydrogen generation. The mechanical response of such igneous rocks (granite and ultramafic rocks alike) to rapid thermal shock remains poorly constrained by experimental data. Many prior studies focus on mechanical or hydraulic stimulation in isolation, while fewer provide paired pre- and post-treatment measurements linking microstructural damage to changes in elastic properties (Zhang et al., 2017). This limitation introduces uncertainty in thermo-hydro-mechanical (THM) models used to predict fracture propagation, stimulated reservoir volume, and long-term reservoir performance in EGS (McClure & Horne, 2014; Elsayed et al., 2024; Rutqvist, 2017).

This study addresses this gap through a controlled laboratory investigation of thermal shock effects on granite and ultramafic rocks. The combination of pre- and post-treatment micro-computed tomography (micro-CT) imaging with non-destructive geomechanical measurements and limited destructive testing, enables the quantification of how a single thermal shock event alters fracture development, porosity, and elastic properties. The resulting dataset provides experimentally grounded constraints for THM modeling and improves understanding of how injection temperature influences mechanical degradation and permeability enhancement in igneous rock systems.

2. EXPERIMENTAL METHODOLOGY

2.1 Specimen Description

The experimental program was conducted on two igneous rock types relevant to Enhanced Geothermal Systems and hydrogen generation systems: granite and ultramafic rock respectively. Cylindrical core specimens were prepared with nominal dimensions of 1.5 inches in diameter and 3 inches in length, consistent with standard rock mechanics testing requirements. A total of four specimens were used for each lithology to establish baseline properties, apply controlled thermal shock treatments, and evaluate post-treatment mechanical and microstructural changes.

To maintain consistency across lithologies, the same labeling convention was applied to both granite and ultramafic samples (e.g., G-3 to G-6 for granite and UM-2 to UM-6 for ultramafic). Prior to testing, all specimens were visually inspected to confirm intact geometry, smooth cylindrical surfaces, and the absence of macroscopic defects.

2.2 Baseline Characterization

Baseline characterization was performed to establish the initial mechanical and microstructural state of each rock type. One specimen from each lithology (G-6 and UM-6) was designated as the baseline reference and used to quantify intact elastic properties prior to thermal treatment. Non-destructive geomechanical measurements were conducted to determine Young's modulus, Poisson's ratio, and bulk modulus, providing reference values for post-shock comparison.

To characterize initial microstructure each specimen was scanned using micro-computed tomography (micro-CT). These scans provided three-dimensional visualization of pre-existing microcracks and pore space, allowing baseline porosity and fracture distribution to be quantified before thermal exposure.

2.3 Thermal Shock Treatment

Thermal shock conditions were designed to simulate cold-fluid injection into hot geothermal reservoirs. Three specimens from each lithology were heated in a laboratory oven to 200 °C for 24 hours. After thermal equilibration, samples were subjected to one of the following treatment conditions:

- **Cold quench:** Instantaneous immersion in **0 °C** water **(UM-3, G-3)**
- **Moderate quench:** Instantaneous immersion in **20 °C** water **(UM-2, G-4)**
- **Heating only:** Heated to 200 °C with no water quenching **(UM-5, G-5)**

The quenching process was rapid and instantaneous, intended to impose a sharp temperature drop and induce thermal shock. During cold quenching, visible gas bubbles formed on the specimen surfaces, indicating rapid microcrack opening, the release of trapped air, and instantaneous boiling of the water.

Figure 1: Granite (left) and ultramafic (right) core specimens used for thermal shock experiments following heating to 200 °C.

Figure 2: Rapid water quenching of a granite specimen after heating to 200 °C.

2.4 Post-Treatment Microstructural Analysis

Following thermal treatment, micro-CT imaging was repeated on the specimens adjacent to the pre-treatment scan locations. Identical scanning parameters were used for all pre- and post-treatment scans to ensure consistency between datasets. The resulting volumetric images were analyzed to assess changes in fracture density, pore connectivity, and total porosity for both granite and ultramafic samples.

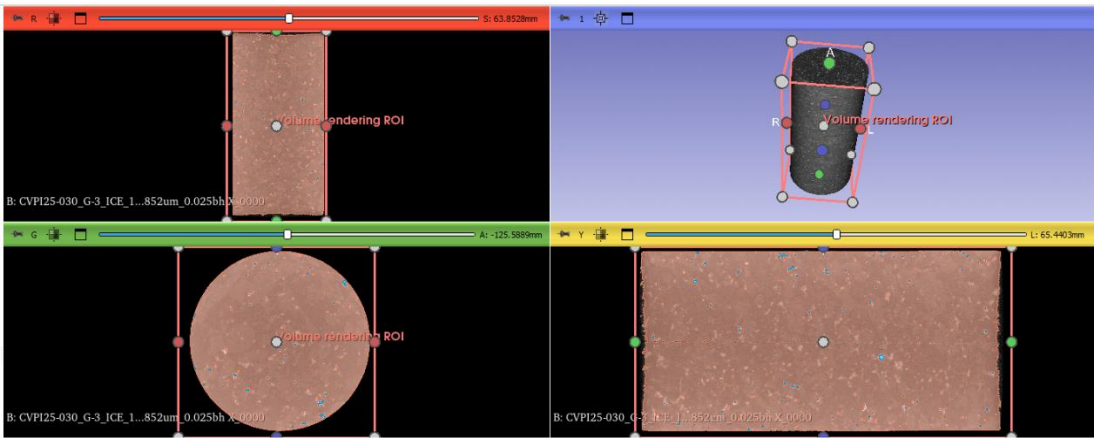

Figure 3: Micro-CT views showing the region of interest (ROI) selected for porosity analysis in a granite sample.

2.5 Geomechanical Testing

Post-treatment geomechanical characterization focused on quantifying stiffness degradation while minimizing additional damage to the specimens. Non-destructive measurements were used to determine Young's modulus and Poisson's ratio after thermal shock, enabling direct paired comparison with baseline values for each lithology. This combined approach enabled quantification of mechanical degradation while preserving most samples for imaging, validation, and future testing.

2.6 Sample Conditions and Testing Summary

Table 1 summarizes the thermal conditions applied to each granite and ultramafic specimen and the corresponding mechanical and petrophysical measurements performed. The experimental workflow is illustrated in Figure 4, which outlines the sequence of baseline characterization, thermal shock treatment, and post-treatment testing. Samples were classified into four thermal states: baseline (no thermal treatment), heating only at 200 °C, rapid quenching in 20 °C water, and rapid quenching in 0 °C water. This design enabled systematic evaluation of increasing thermal shock severity across both lithologies.

As shown in Figure 4, baseline measurements were first conducted to establish reference mechanical properties. Three specimens from each lithology were then heated to 200 °C, followed by either immediate water quenching or cooling without quenching, depending on the assigned condition. Post-treatment testing included micro-CT imaging and selected mechanical measurements to capture thermally induced damage.

Young's modulus and bulk modulus were measured for a subset of specimens using non-destructive or minimally destructive techniques, with test selection guided by specimen integrity and data reliability. P-wave and S-wave velocity measurements were performed on

representative samples primarily for validation and cross-comparison with elastic moduli, rather than as a comprehensive dataset. Porosity was quantified for all samples using micro-computed tomography (micro-CT) image analysis, allowing consistent identification of thermally induced void space and microcrack development across the entire sample set.

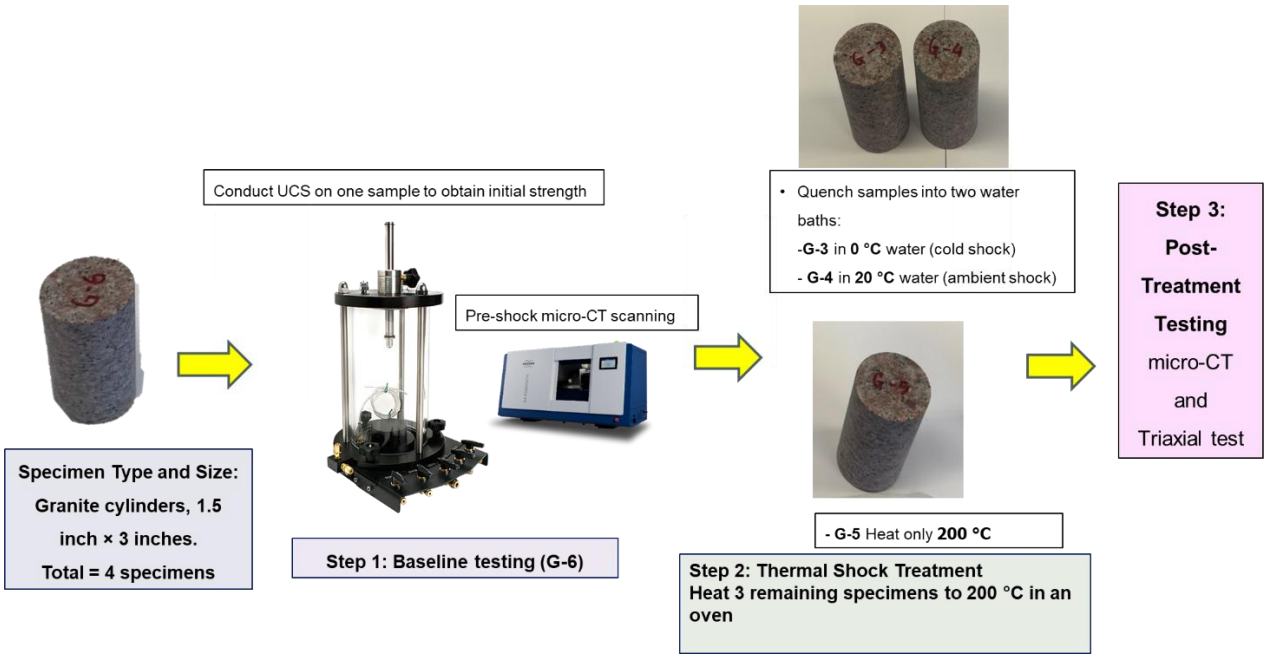

Figure 4: Experimental workflow for thermal shock testing and post-treatment characterization of granite samples.

Table 1: Summary of thermal conditions and completed geomechanical and petrophysical tests for granite and ultramafic samples (✓ indicates test performed).

Sample ID	Condition	Young's Modulus (E)	P- & S-wave velocities (Vp, Vs)	Bulk's Modulus (K)	Porosity (φ)	Triaxial results
UM-2	20 °C shock	✓	✓	✓	✓	✓
UM-3	0 °C shock	✓	✓	✓	✓	✓
UM-5	200 °C only	✓	✓	✓	✓	
UM-6	Baseline	✓	✓	✓	✓	
G-3	0 °C shock	✓	✓	✓	✓	
G-4	20 °C shock	✓	✓	✓	✓	
G-5	200 °C only	✓			✓	
G-6	Baseline	✓			✓	

3. RESULTS

3.1 Porosity Results

3.1.1 Granite Porosity Measurement

Porosity measurements obtained from micro-CT image analysis show a clear dependence of granite porosity evolution on thermal treatment severity (Figures 5–6). The baseline granite sample G-6 exhibits low porosity (~0.80%), providing a stable reference for

assessing thermally induced damage. Heating alone to 200 °C G-5 results in only a minor porosity increase, from 0.81% to 0.88% ($\Delta\varphi \approx +0.07\%$), indicating that uniform heating without quenching produces limited microstructural alteration.

In contrast, samples subjected to thermal shock display larger porosity increases that exceed the heating-only response. The 0 °C quenched sample G-3 shows an increase from 0.68% before treatment to 0.97% after quenching, reflecting enhanced microcrack development associated with rapid cooling. Moderate quenching at 20 °C G-4 produces a smaller but measurable increase in porosity, from 0.90% to 0.99%, remaining above the heating-only baseline.

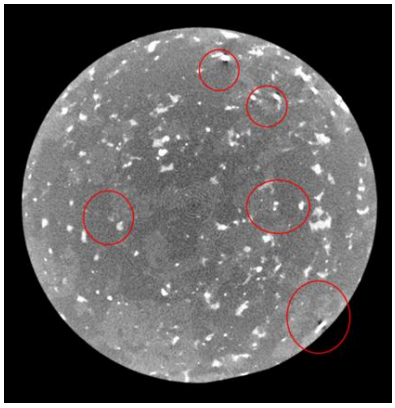

Figure 5: Micro-CT cross-section of granite sample G-3 showing localized pore formation associated with thermally induced microcracking (highlighted by red circles).

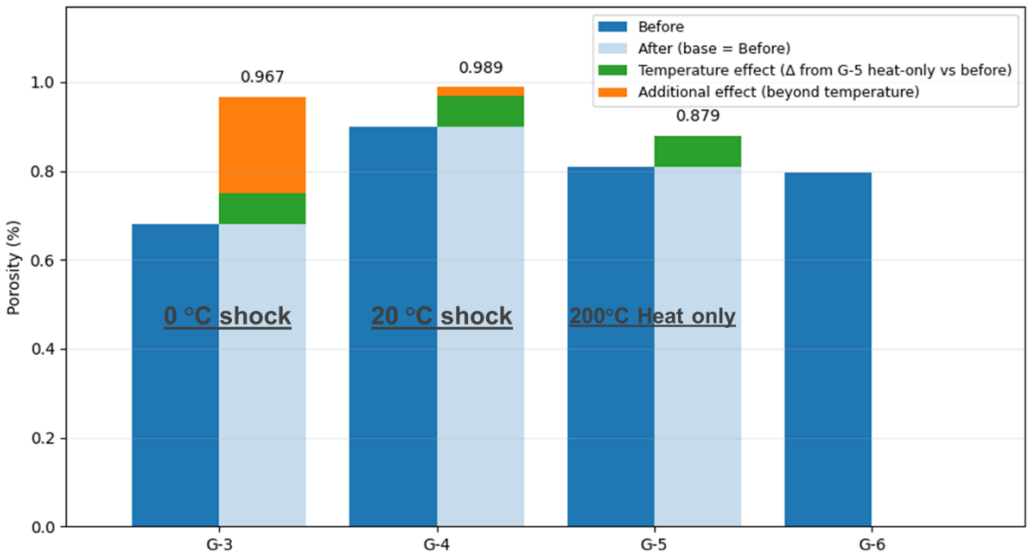

Figure 6: Granite porosity increase separated into heating-only baseline and quenching-induced increase.

3.1.2 Ultramafic Porosity Measurement:

Ultramafic samples displayed higher initial porosity than granite (Figure 7), with baseline values ranging from ~3.0–3.6%, and similarly exhibit porosity increases following thermal shock. Using the heat-only condition UM-5 to isolate the temperature effect, heating to 200 °C produces a porosity increase from 3.63% to 4.06% ($\Delta\varphi \approx +0.43\%$), indicating that the ultramafic rock is more sensitive to heating alone than granite. In contrast, rapid quenching at 0 °C produces larger increases that exceed this heating baseline, with the largest change observed for UM-3 where porosity rises from 3.03% to 4.41%. Samples quenched at 25 °C show moderate increases, including UM-2 (3.11% to 3.55%). The baseline ultramafic sample UM-6 remains stable at ~4.36%. Overall, the ultramafic results demonstrate that both heating and quenching contribute to porosity enhancement, with colder quenching producing the greatest increase. These porosity trends are consistent with thermally induced microcrack opening and provide a microstructural basis for the elastic and velocity changes discussed in subsequent sections.

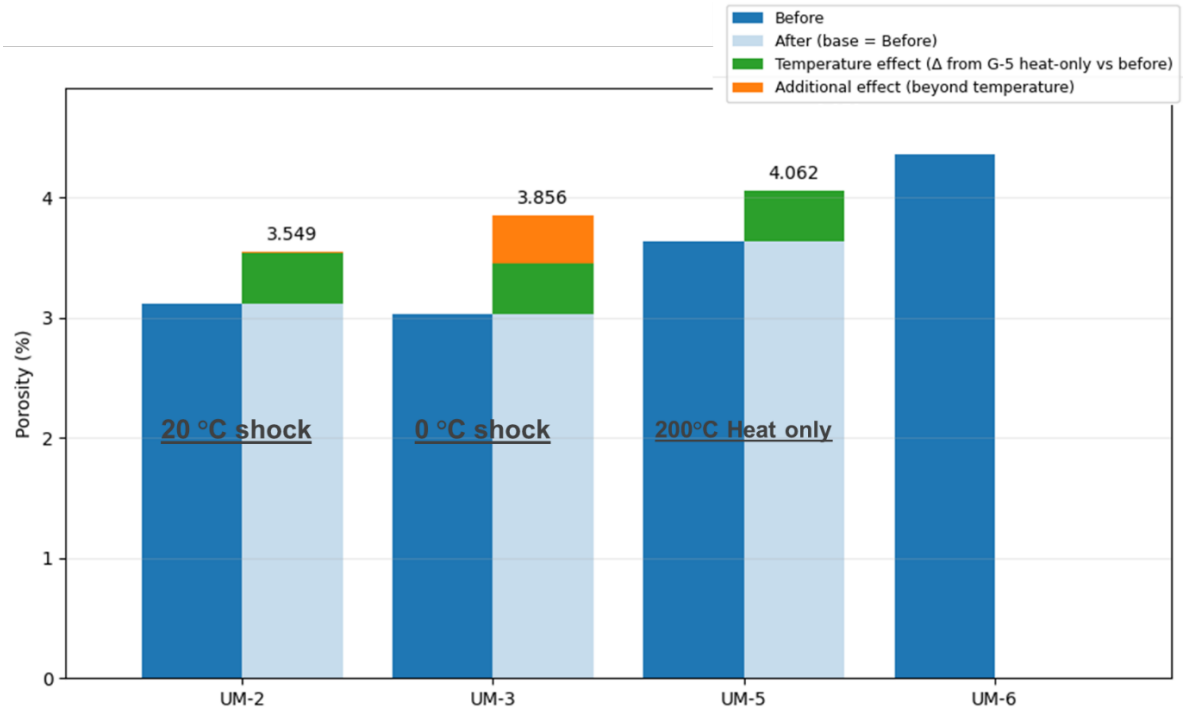

Figure 7: Ultramafic porosity increase separated into heating-only baseline and quenching-induced increase.

3.2 Elastic Wave Velocity and Stiffness Response to Thermal Shock

Post-treatment elastic properties derived from P-wave velocity (Vp), S-wave velocity (Vs), and Young's modulus (E) show systematic variations that are consistent with both lithology and applied thermal shock condition (Figures 8-10). For granite, elastic measurements were obtained for samples G-3 and G-4, corresponding to 0 °C shock and 20 °C shock, respectively.

Sample G-3, subjected to rapid quenching in 0 °C water, exhibits a P-wave velocity of 3396.56 m/s, an S-wave velocity of 1774.29 m/s, and a Young's modulus of 21.68 GPa, representing the lowest stiffness and wave velocities observed among granite specimens. In contrast, sample G-4, quenched in 20 °C water, shows moderately higher elastic properties, with Vp = 3462.30 m/s, Vs = 2050.40 m/s, and E = 27.16 GPa, indicating reduced damage relative to the colder quench condition.

Ultramafic samples consistently exhibit higher elastic wave velocities and stiffness than granite under all tested conditions. Among ultramafic specimens, UM-3 corresponds to a 0 °C shock and displays Vp = 4978.54 m/s, Vs = 3100.40 m/s, and E = 60.38 GPa, while UM-2 (20 °C shock) show slightly lower values, with UM-2 exhibiting Vp = 5089.11 m/s, Vs = 2758.21 m/s, and E = 52.49 GPa. These results indicate that colder quenching generally produces greater elastic degradation, although the magnitude of change is less pronounced than in granite due to the higher inherent stiffness of ultramafic rock.

Samples subjected to heating only (200 °C with no water quench) and baseline conditions retain relatively higher elastic properties. Ultramafic sample UM-5 (200 °C only) exhibits the highest measured stiffness and wave velocities, with Vp = 5499.54 m/s, Vs = 3069.10 m/s, and E = 63.21 GPa, indicating minimal damage from thermal expansion alone. Similarly, the baseline ultramafic sample UM-6 shows intermediate values (Vp = 5223.56 m/s, Vs = 2838.71 m/s, E = 55.42 GPa), consistent with limited pre-existing damage.

Across all samples, reductions in Young's modulus closely track decreases in both P-wave and S-wave velocities, confirming strong coupling between dynamic elastic measurements and bulk stiffness. The lowest elastic properties are consistently associated with rapid quenching at 0 °C, while moderate quenching and heating-only conditions produce progressively less degradation. These results demonstrate that thermal shock severity directly governs elastic property degradation and validate the use of non-destructive elastic wave measurements for quantifying thermally induced damage in crystalline igneous rocks relevant to enhanced geothermal systems.

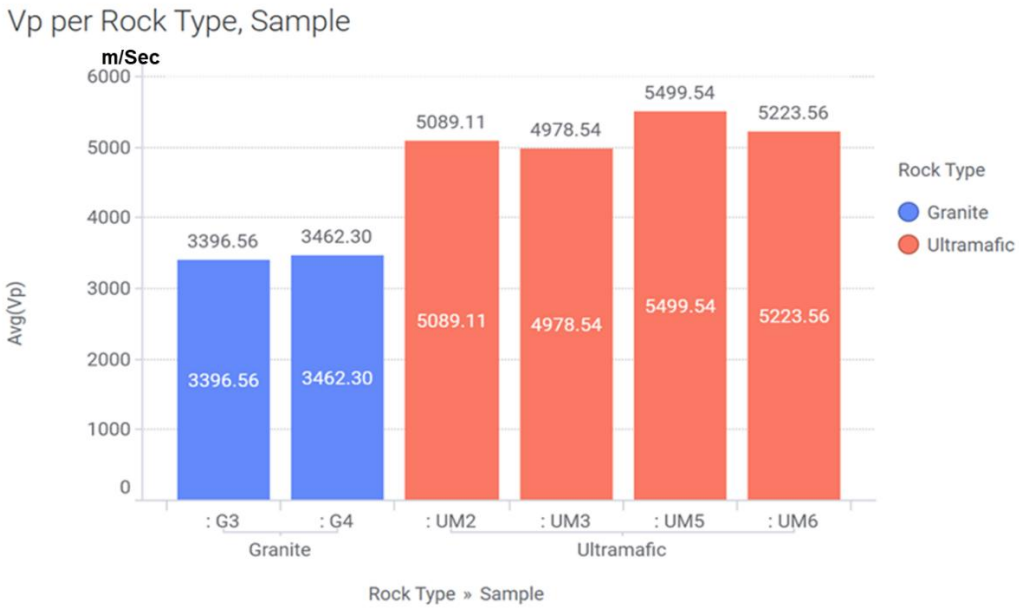

Figure 8: Average P-wave velocity (Vp) for granite and ultramafic samples by sample ID after thermal treatment.

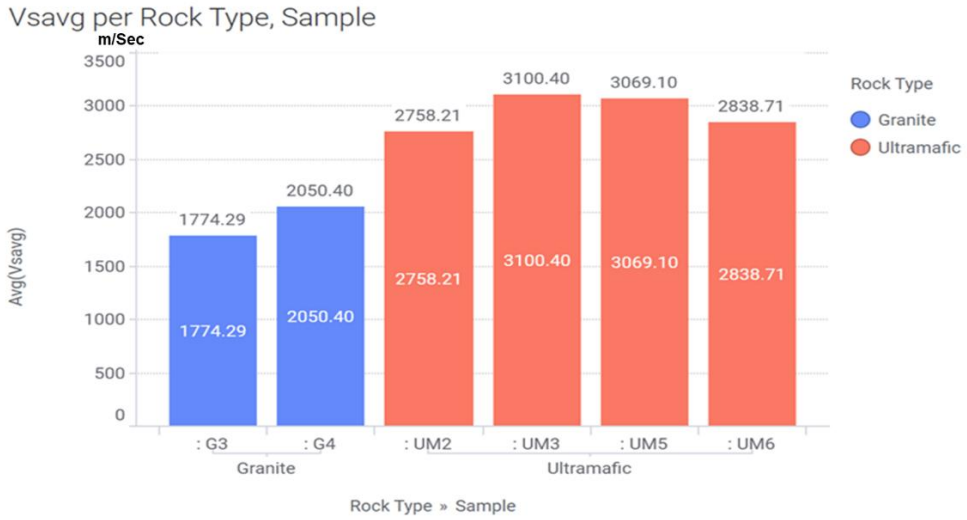

Figure 9: Average S-wave velocity (Vs) for granite and ultramafic samples by sample ID after thermal treatment.

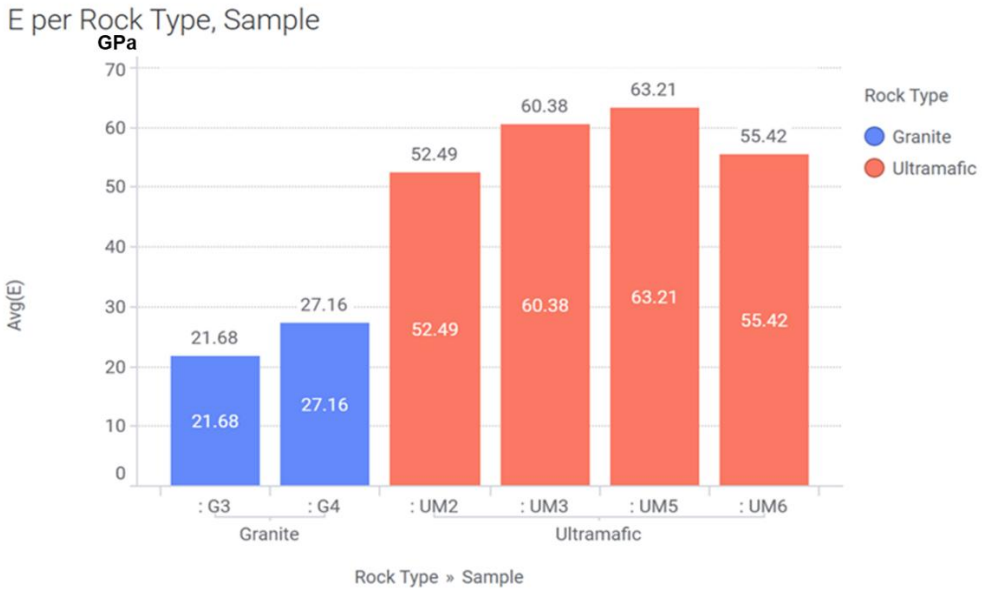

Figure 10: Dyanmic Young's modulus (E) for granite and ultramafic samples by sample ID after thermal treatment.

The dataset summarized in Table 2 is consistent with the trends observed in the preceding figures and highlights the influence of thermal condition and lithology on elastic and seismic properties. For granite, samples subjected to thermal shock exhibit relatively low acoustic velocities and elastic stiffness, with the 0 °C–quenched sample (G-3) showing the lowest Young's modulus (21.68 GPa) and reduced P- and S-wave velocities (3396.56 m/s and 1774.29 m/s, respectively), indicating pronounced microcrack damage under severe thermal shock. The granite sample quenched at 20 °C (G-4) exhibits higher velocities and stiffness (Vp = 3462.30 m/s, Vs = 2050.40 m/s, E = 27.16 GPa), suggesting less extensive damage.

Ultramafic samples consistently display higher P- and S-wave velocities and Young's moduli across all thermal conditions, reflecting their inherently stronger and stiffer mineral framework. The ultramafic specimen subjected to 0 °C shock (UM-3) shows reduced stiffness relative to the heated-only and baseline cases (E = 60.38 GPa), while the heated-only sample (UM-5) exhibits the highest Young's modulus (63.21 GPa) and P-wave velocity (5499.54 m/s). The baseline ultramafic sample (UM-6) retains high velocities and stiffness (Vp = 5223.56 m/s, Vs = 2838.71 m/s, E = 55.42 GPa), serving as a reference for undamaged conditions. Overall, the values in Table X reinforce the observed relationship between increasing thermal shock severity and reductions in elastic and seismic properties, with granite exhibiting greater sensitivity to thermal damage than ultramafic rock.

Table 2: Measured P-wave velocity, S-wave velocity, and Dynamic Young's modulus for granite and ultramafic samples under different thermal shock conditions.

Sample ID	Rock Type	Thermal Condition	P-wave Velocity Vp (m/s)	S-wave Velocity Vs (m/s)	Dynamic Young's Modulus E (GPa)
G-3	Granite	0 °C shock	3396.56	1774.29	21.68
G-4	Granite	20 °C shock	3462.3	2050.4	27.16
UM-2	Ultramafic	20 °C shock	5089.11	2758.21	52.49
UM-3	Ultramafic	0 °C shock	4978.54	3100.4	60.38
UM-5	Ultramafic	200 °C only	5499.54	3069.1	63.21
UM-6	Ultramafic	Baseline	5223.56	2838.71	55.42

3.3 Triaxial Testing Results

3.3.1 Testing condition

Triaxial tests featuring cyclic deviatoric loading at constant confining pressure were conducted enabling the measurement of static elastic properties and observe the accumulation of non-recoverable deformation. Figure 11 shows the testing conditions. UM-2 (20 °C) and UM-3 (0 °C) were tested under the same confining pressure and cyclic deviator-stress loading path to ensure that any differences in mechanical response are attributable to thermal-shock condition rather than loading variability. The applied stress path consisted of: (i) a confining pressure of ~2,500 psi, (ii) cyclic deviator-stress loading to peak values of ~15,000 psi, and (iii) five loading–unloading cycles (Cycles 1–5).

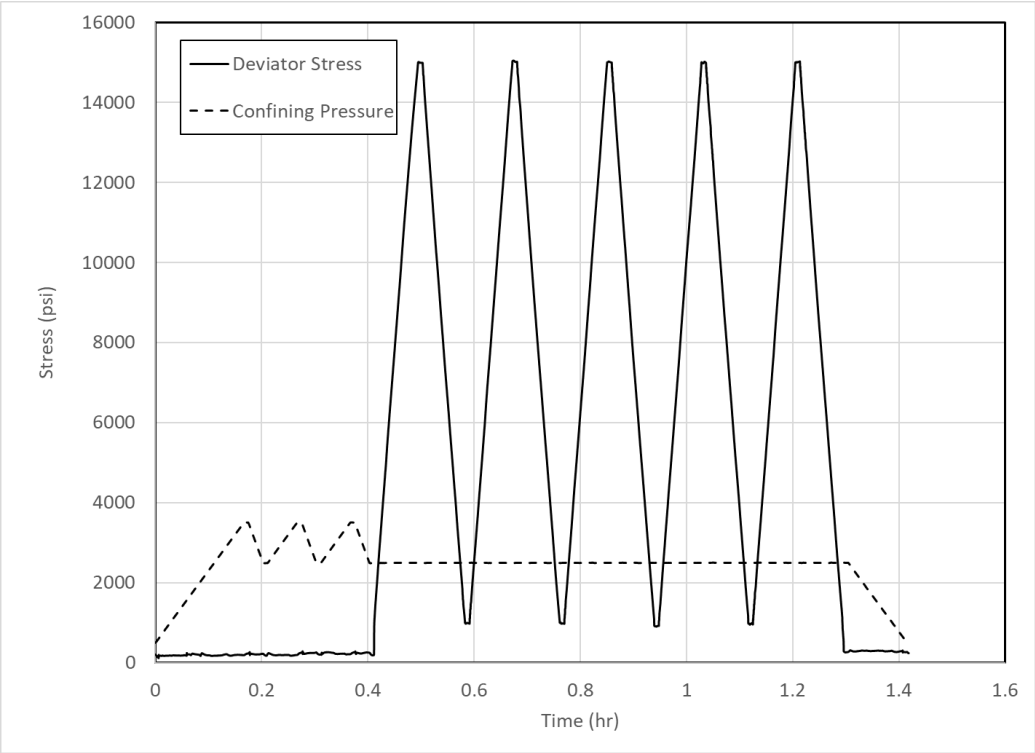

Figure 11: Triaxial Testing cycle

3.3.2 Strain Vs Time

Figure 12 compares axial strain evolution with time for ultramafic samples UM-2 (20 °C shock) and UM-3 (0 °C shock) during cyclic triaxial loading. Both specimens exhibit repeatable strain oscillations associated with applied deviator stress cycles; however, UM-3 consistently develops higher peak axial strain amplitudes and greater residual strain after unloading. The increased axial deformability and reduced strain recovery observed in UM-3 indicate enhanced compliance and progressive damage accumulation relative to UM-2. This behavior is consistent with the lower Young's modulus and altered wave velocities measured for UM-3 and reflects the stronger thermo-mechanical degradation induced by the more severe thermal shock condition.

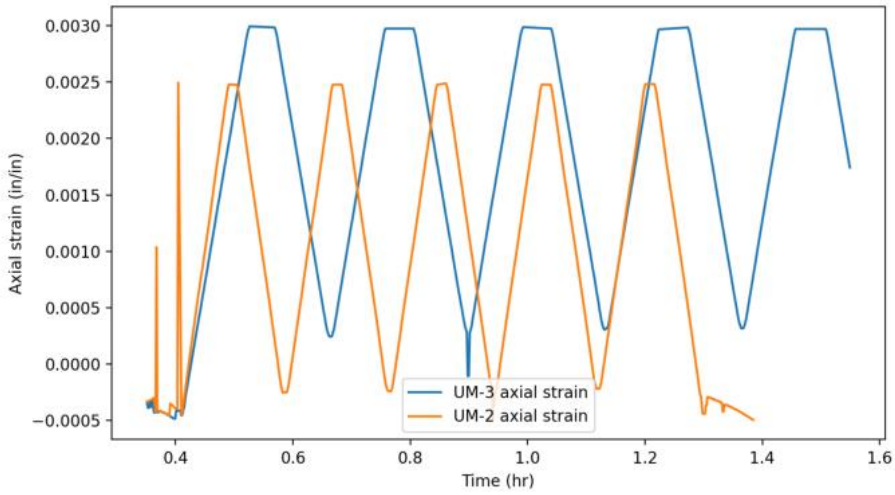

Figure 12: Axial strain vs time for UM-2 (20 °C shock) and UM-3 (0 °C shock).

3.3.3 Stress Vs Strain

Figure 13 compares the deviator stress–axial strain hysteresis loops of ultramafic samples UM-2 (20 °C thermal shock) and UM-3 (0 °C thermal shock under identical triaxial loading conditions. UM-2 exhibits consistently steeper elastic loading slopes across cycles, indicating higher Young's modulus (≈ 8.3–8.9 × 10^6 psi) and a mechanically stiffer response. In contrast, UM-3 shows reduced elastic slopes (≈ 6.1–6.6 × 10^6 psi), wider hysteresis loops, and greater residual strain after unloading, reflecting increased energy dissipation and irreversible deformation. These features indicate more pronounced microcrack-induced damage in UM-3, consistent with the higher thermal shock severity associated with the 0 °C quench. Overall, the hysteresis response demonstrates that colder thermal shock leads to greater mechanical degradation and reduced stiffness in ultramafic rocks.

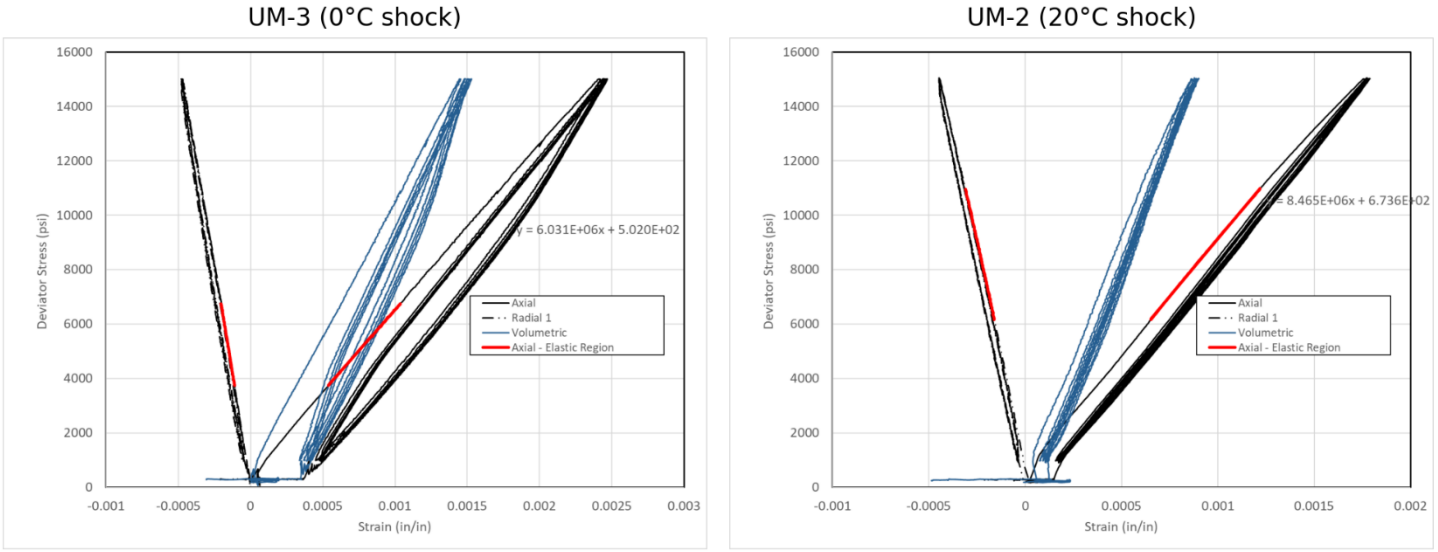

Figure 13: stress–axial strain hysteresis loops for ultramafic samples UM-3 (0 °C thermal shock) and UM-2 (20 °C thermal shock), highlighting differences in elastic stiffness.

4. CONCLUSION

This study investigated the mechanical and microstructural responses of granite and ultramafic rocks to controlled thermal-shock conditions relevant to Enhanced Geothermal Systems (EGS) and hydrogen generation. The experiments provide direct experimental constraints on how injection temperature influences elastic degradation and damage evolution in crystalline rocks by combining micro-CT–derived porosity measurements, ultrasonic velocity data, and cyclic triaxial testing.

Micro-CT analysis revealed systematic porosity increases following thermal treatment in both lithologies, with larger porosity increments observed after colder quenching. These increases are attributed to thermally induced microcracking, primarily along grain boundaries and pre-existing defects. Ultramafic samples consistently exhibited higher absolute porosity than granite, reflecting inherent lithologic differences, while granite showed a stronger relative sensitivity to thermal shock despite lower baseline porosity.

Ultrasonic measurements showed that P- and S-wave velocities, as well as Young's modulus, were consistently higher in ultramafic samples than in granite under comparable conditions. However, samples subjected to colder thermal shock exhibited reduced elastic stiffness relative to warmer shock or baseline conditions. In particular, UM-3 (0 °C shock) showed lower elastic moduli and greater strain accumulation than UM-2 (20 °C shock), indicating enhanced microcrack development under more severe thermal gradients.

Cyclic triaxial testing further highlighted these differences. Stress–strain hysteresis loops demonstrated lower elastic stiffness and greater energy dissipation in the 0 °C–shocked ultramafic sample compared to the 20 °C–shocked sample. The wider hysteresis loops and increased permanent strain in UM-3 indicate more pronounced mechanical damage, while the relatively stable stiffness of UM-2 suggests limited degradation under milder thermal shock. These mechanical observations are consistent with the ultrasonic and micro-CT results, providing a coherent multi-scale interpretation of thermal damage.

Overall, the results confirm that thermal shock severity plays a critical role in controlling microcrack generation, elastic property degradation, and energy dissipation in crystalline reservoir rocks. Colder injection temperatures induce greater mechanical damage, which may enhance permeability but at the cost of reduced stiffness and structural integrity. These findings provide experimentally grounded insight into thermo-mechanical processes in EGS reservoirs and offer valuable constraints for thermo-hydro-mechanical (THM) modeling of reservoir stimulation and long-term performance.

5. ACKNOWLEDGMENTS

The authors gratefully acknowledge **W. D. Von Gonten Engineering LLC** for their support in conducting the laboratory testing and assisting with mechanical measurements. Their expertise and technical support were essential to the successful completion of this study.

REFERENCES

Tester, J.W., Anderson, B.J., Batchelor, A.S., Blackwell, D.D., DiPippo, R., Drake, E.M., et al.: The Future of Geothermal Energy: Impact of Enhanced Geothermal Systems (EGS) on the United States in the 21st Century, MIT Press (2006).

Duchane, D.V., and Brown, D.W.: Hot Dry Rock (HDR) Geothermal Energy Research and Development at Fenton Hill, New Mexico, Geothermics, 31(6), (2002), 643–664. https://doi.org/10.1016/S0375-6505(02)00049-5

McClure, M.W., and Horne, R.N.: An Investigation of Stimulation Mechanisms in Enhanced Geothermal Systems, International Journal of Rock Mechanics and Mining Sciences, 72, (2014), 242–260. https://doi.org/10.1016/j.ijrmms.2014.07.011

Zoback, M.D., Kohli, A.H., Das, I., and McClure, M.W.: The Importance of Slow Slip on Faults During Hydraulic Fracturing Stimulation of Shale Gas Reservoirs, SPE Journal, 17(3), (2012), 1–11.

Yehia, T., Gasser, M., Ebaid, H., Meehan, N., and Okoroafor, E.R.: Comparative Analysis of Machine Learning Techniques for Predicting Drilling Rate of Penetration (ROP) in Geothermal Wells: A Case Study of FORGE Site, Geothermics, 121, (2024), 103028. https://doi.org/10.1016/j.geothermics.2024.103028

Elsayed, T., and Okoroafor, E.R.: Integrated Thermo-Hydro-Chemo-Mechanical (THCM) Analysis for Evaluating CO_2 Plume Geothermal System Potential, Proceedings, SPE Annual Technical Conference and Exhibition, (2024), Paper D031S045R003

Siratovich, P.A., Heap, M.J., Villeneuve, M., Cole, J.W., and Reuschlé, T.: Mechanical Behaviour of Geothermal Rocks Under High-Temperature Conditions, Journal of Volcanology and Geothermal Research, 307, (2015), 109–119. https://doi.org/10.1016/j.jvolgeores.2015.10.003

Griffiths, L., Heap, M.J., Baud, P., and Schmittbuhl, J.: Quantification of Microcrack Characteristics and Implications for Elastic Wave Velocities, Geophysical Journal International, 215(2), (2018), 1015–1030.

Heap, M.J., Faulkner, D.R., Meredith, P.G., and Vinciguerra, S.: Elastic Moduli Evolution and Accompanying Stress Changes During the Onset of Damage in Rocks, Journal of Geophysical Research: Solid Earth, 119(6), (2014), 4939–4959.

Rutqvist, J.: An Overview of TOUGH-Based Geomechanics Models, Computers & Geosciences, 108, (2017), 56–63.

Rutqvist, J., Rinaldi, A.P., Cappa, F., and Moridis, G.: Modeling of Fault Reactivation and Induced Seismicity During Hydraulic Stimulation of Geothermal Reservoirs, Journal of Geophysical Research: Solid Earth, 121(10), (2016), 7252–7276.